# Experimental Demonstration of a Resolution-Enhanced Loop-Terminated Mach–Zehnder Interferometer Narrow Band Fourier Transform Spectrometer

Jianhao Shen, *Student Member, IEEE*, Daniel Donnelly, and Swapnajit Chakravarty, *Senior Member, IEEE*

***Abstract*—We experimentally demonstrate a compact on-chip narrowband Fourier Transform spectrometer (FTS) based on spatially heterodyned array of loop-terminated Mach-Zehnder interferometers (LT-MZIs) in a foundry fabricated silicon-on-insulator (SOI) platform for chip-integrated sensing applications. We demonstrate that LT-MZIs with the same progressive geometric path length difference between the spatially heterodyned arrayed interferometer arms, as in Mach-Zehnder interferometers (MZIs), double the optical phase delay and thus double the wavelength resolution compared to MZIs. Our proof-of-concept device demonstrates one method to address the bandwidth-resolution-compactness tradeoff inherent in on-chip FTSs. The resolution enhancement is significant for optical sensing applications in biosensing and chemical sensing requiring single digit picometers resolution within a narrow wavelength bandwidth in compact on-chip form factors. We discuss the challenges arising from fabrication imperfections in spatially heterodyned FTS in foundry fabricated chips. We propose a method to compensate for phase errors arising from fabrication imperfections within a narrow wavelength bandwidth in the FTS using the refractive index changes in the amorphous to crystalline phase transformations of phase change materials (PCMs), which would enable zero active power consumption during on-chip narrowband FTS operation.**

***Index Terms*—Fourier transform spectrometer, integrated photonics, loop-terminated Mach–Zehnder interferometer, on-chip, phase change materials, phase error compensation, spectrometer.**

## I. Introduction

SPECTROMETERS are significant fundamental instruments in diverse applications ranging from environmental monitoring and biological sensing in healthcare to telecommunication networks and space instrumentation [1], [2]. With the ever-increasing need for miniaturization, portability, performance and cost of ownership for handheld, or unmanned airborne applications, there is a growing need to miniaturize benchtop optical spectrometers to semiconductor chip dimensions to overcome challenges associated with size, weight, and fragile optical alignment sensitivities to environmental fluctuations in benchtop spectrometers. Over the past two decades, integrated photonics have made significant strides towards the demonstration of on-chip spectral decomposition using dispersive methods in arrayed waveguide gratings (AWGs) [3], echelle gratings [4], and meta-surfaces [5] which require one or more sensitive photodetectors to measure individual wavelengths in the optical spectrum. The growing maturity of the silicon photonics platform together with the higher refractive index contrast in a silicon-on-insulator (SOI) platform versus III-V platforms, has enabled further miniaturization of the fundamental components.

In addition to dispersive spectroscopy, Fourier transform (FT) spectroscopy (FTS) has also successfully decomposed a broadband wavelength source into its individual components. In recent years, various FTS methods such as planar waveguide spatial heterodyne spectroscopy (SHS), microring resonator assisted FTS and two-dimensional FTS have been proposed and experimentally demonstrated as an alternative to AWGs and waveguide echelle gratings [6], [7], [8], [9], [10], [11]. In planar waveguide SHS, the moving interferometer arm in bulk optics FT spectrometers is substituted by an array of planar waveguide interferometers, typically in the unbalanced Mach-Zehnder interferometer (MZI) configuration, with increasing phase delays between the interferometer arms on different MZIs in the array [7]. The frequency of periodic transmissions in an individual MZI as a function of wavelength increases with increasing phase delay in the spatially distributed power pattern observed across the outputs of the successive MZIs [7]. As a result, achieving larger wavelength resolution requires longer unbalanced lengths in the array of MZIs. At the same time, spectrometers should ideally cover a large optical wavelength bandwidth. The requirements of wavelength range and wavelength resolution, the constraints on the number of interferometer sampling points placed by the Fourier sampling theorem together with factors such as waveguide propagation loss and available space on a chip limits the number of MZIs that can be arrayed as well as the magnitude of interferometer waveguide arm length imbalance [7]. Demonstration of broadband spectroscopy using spatial heterodyning with chip integrated waveguides requires stringent control on waveguide fabrication to avoid phase errors

Received 18 April 2024; revised 31 July 2024; accepted 16 August 2024. Date of publication 21 August 2024; date of current version 2 January 2025. This work was supported by the National Science Foundation (NSF) under Grant 2210707. *(Corresponding author: Swapnajit Chakravarty.)*

The authors are with the Department of Electro-Optics and Photonics, University of Dayton, Dayton, OH 45469 USA (e-mail: shenj5@udayton.edu; donnellyd4@udayton.edu; schakravarty1@udayton.edu).

Color versions of one or more figures in this article are available at https://doi.org/10.1109/JLT.2024.3447349.

Digital Object Identifier 10.1109/JLT.2024.3447349

arising from fabrication imperfections, as also a consideration of waveguide dispersion in the spectral reconstruction.

While broadband operation is desirable in analyte spectroscopy using Raman or Fourier methods, it is not required for many narrowband single-wavelength resolving applications [12], [13], [14] where high resolution is more important. Applications where narrow-band spectroscopy is sufficient include biosensing where one measures $\delta\lambda\sim$1pm resolution in a $\Delta\lambda$ = 1–2 nm bandwidth to achieve the lowest LODs [15], [16], and gas sensing that need $\delta\lambda\sim$0.6 nm resolution in a $\Delta\lambda = 2$ nm bandwidth to detect gas isotopes for example [14]. Furthermore, in such applications, a single resonance lineshape such as in a microcavity resonator or a single narrow absorbance lineshape needs to be monitored for changes. One method to double the spectrometer resolution is to double the path length difference in each MZI for a fixed number of unbalanced MZIs. In this paper, we propose and experimentally demonstrate a compact narrow band loop-terminated Mach-Zehnder interferometer-based Fourier transform spectrometer (FTS) in which an unbalanced LT-MZI array achieves twice the wavelength resolution of an equivalent unbalanced MZI array with the same geometric path length difference between the interferometer arms.

An ideal on-chip spectrometer using spatial heterodyning assumes that the optical path length difference between the spatially heterodyned arms is an integral multiple of the smallest optical phase delay. While the silicon photonics foundry is mature, effective indices of waveguide modes are extremely sensitive to small variations in the waveguide width and device silicon height, as also the etched waveguide sidewall angle, across a wafer. As the geometric path length is increased to achieve higher wavelength resolution, there is a potential increase in phase errors due to fabrication imperfections. On-chip heaters can compensate for phase errors arising from fabrication imperfections using the thermo-optic effect [17]. As spectrometer size increases to achieve higher resolution, the number of heaters multiply by the same factor thereby increasing power consumption. Moreover, the heater needs to be ON at all times during active operation thus presenting a significant active power consumption. In recent years, phase change materials (PCMs) based on various chalcogenides have shown large refractive index changes during the amorphous to crystalline phase transformation and vice-versa [18], [19]. The phase transformation is non-volatile, implying that the index change is permanent until a reset pulse is applied. It is possible to tune PCMs into several intermediary material states, implying a continuous tuning of the refractive index [20], [21].

In on-chip FT spectrometers, PCM integration with on-chip waveguides can tune the waveguide effective index and phase delay for fabrication induced phase error correction. In this paper, we show via device modeling how a representative PCM ($Sb_2Se_3$, antimony selenide) can potentially tune the FT interference fringes. Mathematical methods for correction in the literature such as compressed sensing ideally require spectrally sparse signals [22] for efficient spectral decomposition or narrow band optical filters for broadband sources to estimate the background. Matrix inversion methods [23] require wavelength sampling during calibration and represent a software driven method to correct

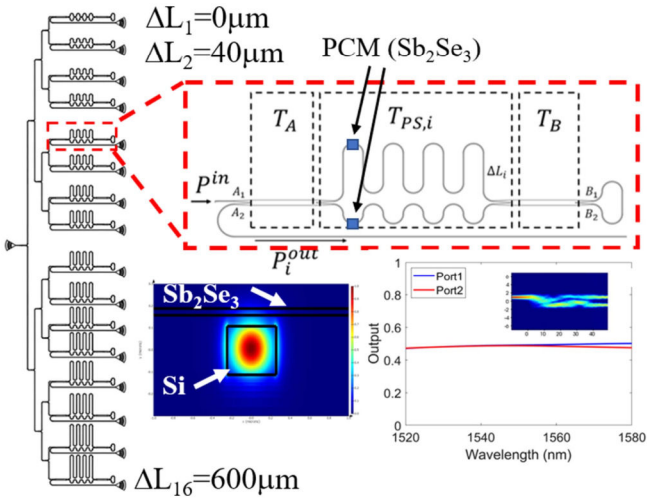


Fig. 1. Schematic of LT-MZI FTS, with each stage labelled with its respective transfer matrix. Dashed red inset shows proposed PCM integration on one of the interferometer arms. Optical mode profile is shown in bottom left inset with integrated PCM. Bottom right inset shows the transfer function and mode splitting of the 2 × 2 MMI splitter.

phase errors. Recently, stationary wave integrated FT systems have demonstrated a lot of promise for large bandwidth FTS, however they are still limited by large size exceeding 20mm$^2$ while achieving a resolution >1nm with off-chip interferogram readout [24]. In a narrow spectral bandwidth however, waveguide dispersion can be ignored [7], and an average refractive index assumed for spectral reconstruction.

Fig. 1 shows a schematic drawing of the proposed FT spectrometer with an array of 16 unbalanced loop-terminated Mach-Zehnder interferometers. A light source at an input grating coupler (GC) is split into 16 paths with a 4-stage cascaded tree of 1 × 2 power splitters. In the last stage, in contrast to the MZI array, an input to port $A_1$ of a 2 × 2 multimode interferometer (MMI) power splitter, $\text{MMI}_\text{A}$, splits the power into the two unbalanced arms of the interferometers. The ports $B_1$ and $B_2$ are connected via a loop waveguide mirror which reflects the light back to the unbalanced interferometer arms. The output light that exits through $A_2$ is measured at the output GCs. Since the light is reflected by the loop mirrors, it travels an effective path length that is twice that of an equivalent MZI with the same geometric length of the interferometer arms. As a result, the phase delay in the LT-MZI is doubled compared to the equivalent MZI leading to double the resolution versus the MZI.

## II. Mathematical Model

The mathematical model of the arrayed LT-MZI can be intuitively described using transfer matrices [7]. Considering $a$ and $b$ as coupling coefficients, the transfer matrix of both MMI couplers can be expressed as:

$$T_{mmi} = \begin{bmatrix} a & jb \\ jb & a \end{bmatrix} \tag{1}$$

The coupling coefficients are dependent on multiple factors, including how much loss the MMI experiences and how exactly

the power is split between the ports. For a lossless MMI coupler, $a^2 + b^2 = 1$, and if the coupler has accurate 3dB splitting and a 90-degree phase shift between the outputs, $a = b = \frac{1}{\sqrt{2}}$. Assuming both of these conditions, and considering the naming convention of each of the MMI's in Fig. 1, (1) can be rewritten:

$$T_{mmi} = T_A = T_B = \frac{1}{\sqrt{2}} \begin{bmatrix} 1 & j \\ j & 1 \end{bmatrix} \tag{2}$$

where $T_A$ and $T_B$ are represent transfer matrices of the first MMI ($MMI_A$) and second MMI ($MMI_B$) respectively. For the middle phase shifting section of the device [7], the transfer matrix $T_{PS,i}$ is shown below in (3):

$$T_{PS,i} = \begin{bmatrix} e^{j\phi_1} & 0 \\ 0 & e^{j\phi_2} \end{bmatrix} = e^{j\phi_2} \begin{bmatrix} e^{j\Delta\phi,i} & 0 \\ 0 & 1 \end{bmatrix} \tag{3}$$

Here, $\Delta\phi_i$ is the phase difference between the two interferometer arms of the $i$th LT-MZI. This phase difference can be rewritten as $\Delta\,\phi_i = \beta\Delta L_i$, where $\beta$ is the propagation constant of the fundamental mode (the transverse electric (TE) mode in our device) and $\Delta L_i$ is the interferometer path length difference. The power at the ports $B_1$ and $B_2$ before the loop mirror to the input power at $A_1$ and $A_2$ can be shown below in (4) as:

$$\begin{bmatrix} B_1 \\ B_2 \end{bmatrix} = T_B\, T_{PS,i} T_A \begin{bmatrix} A_1 \\ A_2 \end{bmatrix} = T_B\, T_{PS,i} T_A \begin{bmatrix} P^{in} \\ 0 \end{bmatrix}$$
$$= \frac{1}{2}\, e^{j\phi_2} \begin{bmatrix} e^{j\Delta\phi_i} - 1 \\ j\left(1 + e^{j\Delta\phi_i}\right) \end{bmatrix} \tag{4}$$

On the forward path, as in an MZI, the outputs oscillate with a frequency determined by the phase difference $\Delta\phi_i$ between the interferometer arms. However, on the reflected (backward) path, the loop mirror switches the output matrix elements so that the transfer matrix relationship can be written as:

$$\begin{bmatrix} A_1 \\ A_2 \end{bmatrix} = T_A\, T_{PS,i} T_B \begin{bmatrix} B_2 \\ B_1 \end{bmatrix} = \frac{1}{2}\, e^{j\phi_1} \begin{bmatrix} j\left(e^{2j\Delta\phi_i} - 1\right) \\ -\left(1 + e^{2j\Delta\phi_i}\right) \end{bmatrix} \tag{5}$$

As observed from (5), the reflected light at $MMI_A$ on both arms $A_1$ and $A_2$ oscillates at a frequency of $2\Delta\,\phi_i = 2\beta\Delta L_i$. An optical circulator in our experiments connected to the input fiber prevents reflection back to the source. The lower output $A_2$ is monitored to determine the output of the LT-MZI, for all 16 unbalanced LT-MZIs in the demonstrated spectrometer. From (5), the reflected powers $P^{out}$ at the two arms of $MMI_A$ for a monochromatic signal back to the input 2 × 2 MMI are related to the input power $P^{in}$ by (6) and (7) as:

$$P^{out}_{A_1}\,(x_i) = \frac{1}{2}\, P^{in}\left[1 - \cos 2\beta\Delta L_i\right] \tag{6}$$

$$P^{out}_{A_2}\,(x_i) = \frac{1}{2}\, P^{in}\left[1 + \cos 2\beta\Delta L_i\right] \tag{7}$$

For a polychromatic signal input [9], ignoring dispersion over a narrow wavelength bandwidth [7], the input spectrum is obtained from the measured interferogram using the discrete Fourier transform that is given by:

$$P^{in}\,(\bar{\sigma}) = \frac{\Delta x}{N}\, P^{in} + 2\frac{\Delta x}{N} \sum_{i=1}^{N} W\,(x_i)\, F\,(x_i) \exp j2\pi\bar{\sigma}\,(2x_i) \tag{8}$$

where $F(x_i) = 2P_i^{out} - P^{in}$, assuming an ideal 3dB splitting in a lossless MMI coupler. $N$ represents the number of interferometer arms, $\bar{\sigma} = \sigma - \sigma_{\min}$ represents the wavenumber $\sigma$ shifted from a minimum wavenumber $\sigma_{\min}$ at the Littrow condition [7] when phase delays in all the interferometer arms are integral multiples of $2\pi$. A function $W(x_i)$, an apodization function included to reduce ripples caused by the truncation of the spatial interferograms in the DFT, is given by [7]:

$$W\,(x_i) = \left[1 - \left(\frac{x_i}{x_{\max}}\right)^2\right]^2 = \left[1 - \left(\frac{\Delta L_i}{\Delta L_{\max}}\right)^2\right]^2 \tag{9}$$

The maximum geometric path delay [25] of the arrayed LT-MZI with waveguide mode group index $n_g$, $\Delta L_{\max}$, is given by:

$$\Delta\, L_{\max} = \frac{1}{\delta\sigma n_g} \tag{10}$$

The number of unbalanced LT-MZIs and hence the required number of discrete points N in the interferogram is determined by the Fourier sampling theorem from which we obtain

$$N_{\min} = 2\,\frac{\Delta\sigma}{\delta\sigma} = 2\frac{\Delta\lambda}{\delta\lambda} \tag{11}$$

where $\Delta\lambda$ is the wavelength spectral range and $\delta\lambda$ is the wavelength resolution of the spectrometer. It can be seen from (11) that, since the effective maximum path length difference of the LT-MZI is twice that of the MZI, hence $\delta\ \sigma_{LT-MZI} = 0.5(\delta\sigma_{MZI})$.

## III. Device Design and Simulation

Eigenmode simulations were done for the straight and bent waveguides forming interferometer arms, loop mirror waveguide, and 2 × 2 MMI 50:50 splitters. GCs and 1 × 2 50:50 splitters were incorporated from the foundry process development kit (PDK). Our design achieves a wavelength resolution $\delta\lambda$ = 0.48nm, with an incremental path length $\Delta L = 40\ \mu$m over 16 interferometer arms.

The device was simulated in Ansys Lumerical Interconnect for each $\Delta L_i$ in both LT-MZI and MZI configurations. Fig. 2(a) and (b) plot the interference spectra in the 16 arms showing the Littrow wavelengths at which all interferometer arms are in phase. As expected, the Littrow condition repeats with twice the wavelength range in the MZI configuration versus the LT-MZI configuration for the same geometric interferometer arm lengths. The deconvoluted spectra, considering the Nyquist-Shannon sampling theorem, for a monochromatic wavelength in Fig. 3(a) shows the higher resolution achieved in the LT-MZI compared to the equivalent MZI with the same geometric path length difference. The LT-MZI has a smaller ~13cm$^{-1}$ free spectral range (FSR) defined as half the period of the least unbalanced LT-MZI, due to the symmetry of the interferograms. Over the narrow FSR bandwidth $\Delta\sigma$ = 13 cm$^{-1}$, the effective index and group index of the fundamental TE mode vary by $\Delta n_{eff}$<0.004 and $\Delta n_g$<0.0004 respectively. The variation leads to an error in $\delta\lambda$ ~0.08 pm ($\delta\lambda = \lambda_0^2/(\Delta L_{\max} n_g)$), significantly smaller than the FTS resolution here [7] within the FSR. Fig. 3(b)

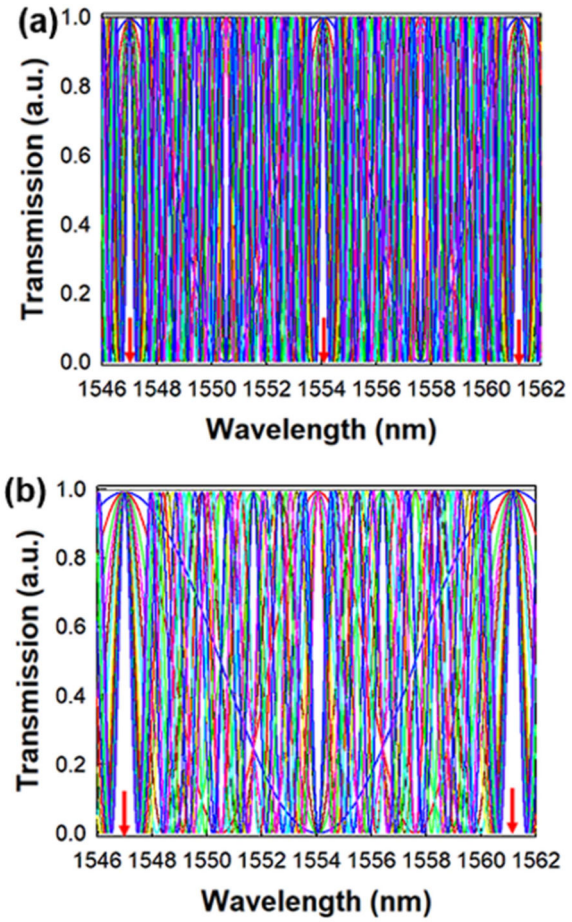


Fig. 2. Simulated interference spectra of 16 arms of the (a) LT-MZI and (b) MZI spectrometer showing Littrow wavelengths (red arrows).

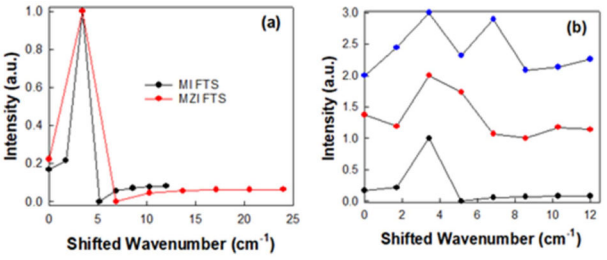


Fig. 3. Reconstructed spectra from simulated circuit showing (a) enhanced resolution of the LT-MZI FTS vs MZI FTS with same geometric path lengths of interferometer arms and (b) ability of LT-MZI FTS to resolve two spectral lineshapes $\Delta\sigma = 3.4$ cm$^{-1}$ ($\delta\lambda = 0.96$ nm) apart at FWHM in blue dots but inability to resolve two lineshapes $\Delta\sigma = 1.7$ cm$^{-1}$ ($\delta\lambda = 0.48$ nm) apart at FWHM in red dots. $\Delta\sigma = 0$ represents the Littrow wavelength ($\sigma = \sigma_{\min}$). Spectra are offset for clarity.

shows that at the full-width half maximum (FWHM), with a wavelength resolution $\delta\sigma = 1.7$ cm$^{-1}$, the designed LT-MZI FTS can identify two input sources that are separated by $\Delta\sigma = 3.4$ cm$^{-1}$. However, when two sources are separated by $\Delta\sigma = 1.7$ cm$^{-1}$, while wavelengths are resolved and a broad peak is observed, the designed LT-MZI FTS cannot uniquely identify them at their FWHM. In such circumstances, typically peak fitting is employed in software. In order to clearly identify the two sources at the FWHM, an additional sampling point is necessary which can be achieved by doubling the number of LT-MZI arms or increasing the number of sampling points in the pseudoinverse matrix method [14].

The reduction in the lateral dimension of the LT-MZI interferometer FTS versus the MZI interferometer FTS is n $\times$ 2r where n is the number of U-turns and r is the bend radius. In our proof-of-concept devices n = 8 and r = 6 $\mu$m making the lateral length reduction 96 $\mu$m. The target resolution in biosensing is typically $\delta\lambda$ = 1–10 pm. [16], [17], [18], [19], [20], [21], [22], [23], [24], [25] Assuming that vertical dimensions remain unchanged, with an incremental path length $\Delta$L = 40 $\mu$m over 16 interferometer arms, the number of U-bends would increase to 600 leading to a lateral length reduction ~7.2 mm. Increasing the number of interferometer arms to 64 would reduce the lateral length to ~1.8 mm while increasing vertical dimension from 1.77 mm to 7.1 mm in the present design. It may be noted that $\delta\lambda$ = 1 pm (= 0.001 nm) and smaller is desired to reach the lowest limits of detection (LOD) [12] at $1 \times 10^{-7}$ RIU (refractive index unit) in chip-integrated chem-bio sensing. A significant compactness can thus be achieved in the loop-terminated Mach-Zehnder FTS configuration versus the commonly used MZI FTS configuration.

Fig. 4(a) plots the spacing of the interference fringes in the 16 LT-MZI FTS arms. Fig. 4(b) shows simulated fringe shift in two interferometer arms with $\Delta$L = 40 $\mu$m and $\Delta$L = 80 $\mu$m, with a 25 nm thick $Sb_2Se_3$ on top of the 500 nm wide silicon waveguide and refractive indices n = 3.25 and n = 4.025 obtained from in-house ellipsometry (and further corroborated by the literature) [26], in the amorphous and crystalline material phases. Fig. 4(c) plots the achievable interference fringe shifts for different lengths of the 500 nm wide $Sb_2Se_3$ PCMs at different heights above the waveguide. Fig. 4(d) plots the representative interference fringe shift for the two least unbalanced arms of the interferometer and the most unbalanced arm (physical $\Delta$L = 600 $\mu$m) as a fraction of the fringe period. It is observed that a 6 $\mu$m long PCM located right on top of the silicon waveguide achieves 50% fringe offset correction for all the interferometer arms. The change in FSR as a result of the phase change at different heights away from the waveguides is indicated in Fig. 4(e). The PCM is to be patterned on both arms, with the same length, as shown schematically in Fig. 1, to ensure propagation loss uniformity in the two interferometer arms. Since fabricated waveguide dimensions and geometry deviate from the ideal rectangular profile, taking potential dimensional guidance from the foundry PDK, we simulated the fringe period in Fig. 4(f) for various geometries of the ridge waveguide to determine the potential waveguide cross-section from the measured interference fringe spacing on the individual arms of the FTS.

$Sb_2Se_3$ integrated silicon waveguides have demonstrated propagation loss <0.006 dB/ $\mu$m [20], in crystalline and amorphous phases. The PCM length ($L_C$) is kept short to achieve the required fabrication imperfection induced phase correction in the interferometer with smallest $\Delta$L which has the smallest fringe spectral sensitivity (fringe shift/free spectral range). At $L_C$ = 4 $\mu$m, the crystalline phase loss in $Sb_2Se_3$ is ~0.05 dB which

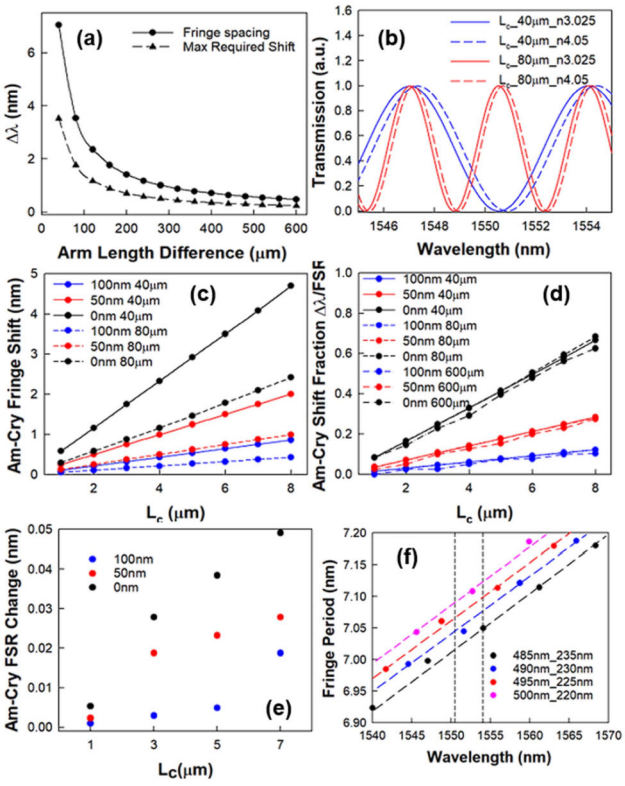


Fig. 4. (a) Fringe spacing and the maximum required adjustment to meet a Littrow condition via PCM tuning. (b) Shift in interference fringes on two adjacent arms with $\Delta L = 40\ \mu m$ (blue) and $\Delta L = 80\ \mu m$ (red) with PCM in amorphous (solid) and crystalline (dashed) material phase. (c) Fringe shift from the amorphous to crystalline (Am-Cry) phase transition for the two smallest unbalanced interferometer arms at different PCM offsets from the top of the waveguide. (d) Fringe shifts from the amorphous to crystalline (Am-Cry) of the least two and the most unbalanced interferometers as a fraction of the fringe period versus length of PCM. (e) Change in FSR on the least unbalanced arm due to amorphous to crystalline (Am-Cry) PCM phase transition vs PCM length at different silicon dioxide ($SiO_2$) separation of PCM above silicon waveguide. (f) Variation of fringe period versus wavelength for different waveguide geometries (bottom width and height) with 85-degree sidewall angle of the least unbalanced arm. The dotted line shows a representative bandwidth of the designed FTS.

translates to ~1% loss induced imbalance that has practically no impact on the spectral reconstruction. We assume, based on multi-level refractive index tuning of $Sb_2Se_3$ demonstrated in refs. [20], [21], that the index of $Sb_2Se_3$ can be continuously tuned to stable intermediate states as shown in Fig. 4(b). For a fixed PCM dimension, if the phase error by PCM index change can be corrected in the interferometer with smallest $\Delta L$, then phase error correction can be easily achieved for the PCM phase shifter of the same length in other arms with longer $\Delta L$.

## IV. Experimental Results

Devices were fabricated in 220 nm thick device silicon in SOI wafers with a 2 $\mu$m thick bottom SiO2. The initial designed single mode waveguide effective refractive index $n_{eff}$ is 2.44 at $\lambda = 1550$ nm. The waveguide bend radius is $r = 6\ \mu m$. The $2 \times 2$ MMI measures $39\ \mu m \times 3.3\ \mu m$. The FTS with all interferometer arms measures 1.8 mm × 0.5 mm. Devices are covered with ~5 $\mu$m thick SiO2.

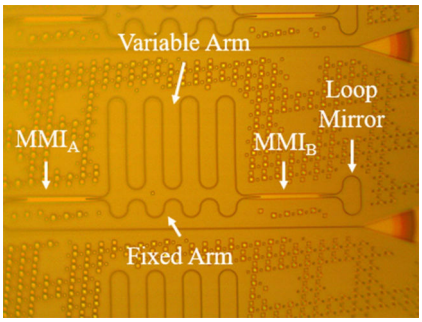


Fig. 5. Microscope view of one of the 16 arms of the LT-MZI FTS.

Fig. 5 shows a zoomed-in image of one unbalanced interferometer in the array, with components shown schematically in Fig. 1. The reconstruction of the input source spectra from experimental measurements presents several challenges that are overcome systematically. Fig. 6(a)–(f) show the raw measured interference fringes observed from the a few selected interferometer arms of the FTS. Additional fringes with higher spatial frequencies are seen superimposed on each fringe spectrum. The higher order fringes, as demarcated in the green dotted regions in Fig. 6(g)–(l), arising from fiber-to-fiber Fabry-Perot effects (as determined from the fringe periodicity) and other sources of noise from the detectors are eliminated by importing the data into Matlab, performing a discrete Fourier transform (DFT) and then taking the inverse transform with a low pass filter. The frequency corrected DFT are shown plotted in red in the insets of Fig. 6(g)–(l) respectively and done for all interferometer arms. For all interferometer arms, in addition to the high fringe periodicity frequencies, a slowly varying envelope is also observed on top of the envelope of the grating coupler input spectra and is plotted in blue in Fig. 6(m)–(r). The slowly varying envelope is identified specifically in the Fourier spectrum of the balanced arm #1 in Fig. 6(g) and (m) and arises from a cavity formed between the 2 MMIs as the light is reflected back by the loop mirror. The corresponding frequency of the slow varying envelope is shown in blue in the insets of Fig. 6(g)–(l). Finally, the DFT corrected interference spectra are shown in Fig. 6(m)–(r). The DFT corrected interference spectra in Fig. 6(m)–(r) are normalized to the slowly varying envelope in each arm in Fig. 6(m) and plotted in Fig. 7(a)–(f), thereby correcting for the Fabry-Perot effects, the cavity formed between the MMIs, detector noise and the coupling efficiency differences of GCs in the 16 arms arising from fabrication offsets across the wafer.

Fig. 7(a)–(f) show representative normalized raw interference fringe spectrum from six arms, measured with a tunable laser. The DFT corrected interference spectra are superimposed in dashed red in Fig. 7(a)–(f). In balanced arm #1 with $\Delta L = 0$, DFT correction and envelope normalization results in a unity corrected value across all wavelengths, as expected for a balanced arm. An investigation of the fringe spacing observed experimentally in the unbalanced arms revealed a deviation of the FSR from the designed FSR that considered an ideal steep 90-degree vertical waveguide sidewall and a waveguide cross section 500 nm × 220 nm. The foundry PDK indicates a sidewall

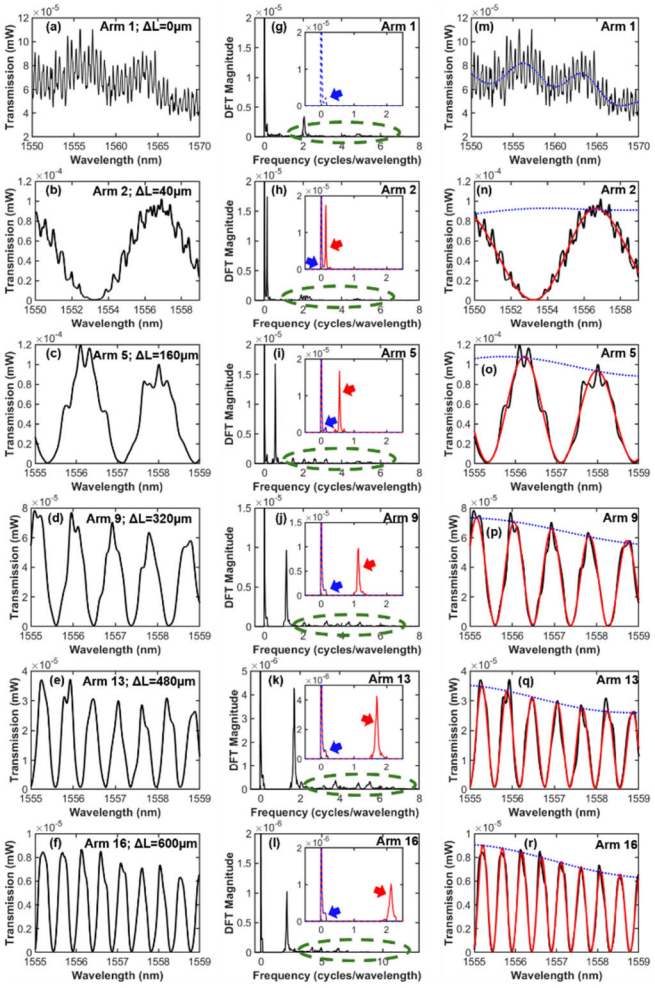


Fig. 6. (a)–(f) Raw experimentally measured interference fringes, and (g)–(l) spatial fringe periodicity DFT of the measured fringes. Corrected DFT filtering higher order frequencies (in green dashes) are shown in the insets (in red) and the slowly varying envelope (in blue dots). The zero-fringe frequency represents the grating coupler envelope. (m)–(r) DFT corrected experimentally measured interference fringes (in red), superimposed on the raw fringes (in black) and slow varying envelope (in blue dots).

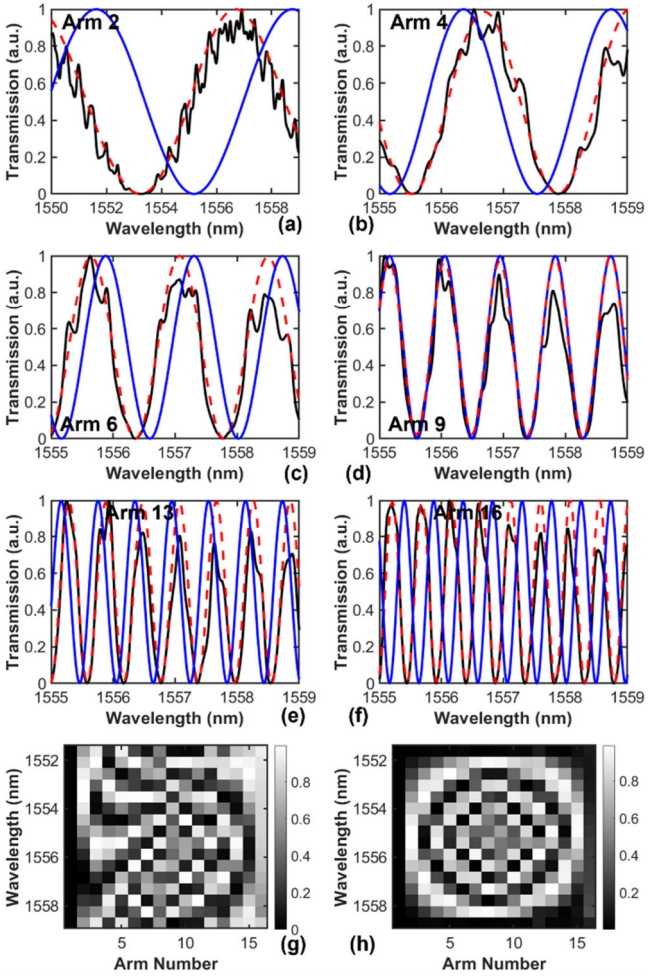


Fig. 7. (a)–(f) Simulated (blue) and measured experimental (black) fringe spectra considering trapezoidal shaped waveguides with bottom width 490 nm, height 230 nm and sidewall angle 85 degree. Arm 9 simulation fringes matched exactly with the measured spectrum. The DFT corrected experimental plots are in red dashes. No phase shifting required in (d) as experiment overlaps with simulation. (g) Normalized power measured versus wavelength at 16 sampling points from the raw unprocessed experimental spectra. (h) Normalized DFT corrected power at the 16 sampling points after offsetting the fringes by phase errors simulated to match experiments in Fig. 4(d).

etch angle of approximately 85-degree. A bottom trapezoidal shaped waveguide width between 485–495 nm, and a waveguide thickness between 225–235 nm matched the FSR best for all the interferometer arms. For this range of dimensions, the maximum FSR variation as noted in Fig. 4(f) is 0.04 nm, an order of magnitude less than the wavelength resolution of our demonstrated FTS. For modeling, the simulated results presented in Figs. 2–4 considered the waveguide geometries with an average width 490 nm and thickness 230 nm. There is always the possibility of waveguide thickness and height variation within the spatial extent of the FTS, as indicated from the representative spectra in Fig. 6 which is another potential benefit in transitioning to a smaller spatial extent in the LT-MZI FTS versus a MZI FTS.

Fig. 7(g) shows the experimental raw measured transmission spectra measured in all 16 arms of the fabricated LT-MZI FTS. Due to phase errors caused by fabrication imperfections, a Littrow wavelength cannot be identified in Fig. 7(g). For a given waveguide cross-section, the Littrow wavenumbers all align in simulation. The phase error between the measured experiment and simulated interference spectra for each arm at the Littrow wavenumber is determined in Ansys interconnect by incorporating an optical phase shifter element in one of the interferometer arms and plotted in Fig. 8 for all the interferometers. Due to the small FSR of our FTS ($\sim$13 cm$^{-1}$), waveguide dispersion can be ignored, as will also be noted later from measurements. The absolute phase errors between a designed waveguide and its fabricated counterpart can be larger than $2\pi$ due to variation in waveguide dimensions. Since the Fourier transform is $2\pi$-periodic, by ignoring dispersion within the small FSR of our narrow-band FTS, the phase errors can be corrected within $2\pi$. The corrected interference fringes can be determined by phase shifting the DFT corrected measured fringes by the results from Fig. 8, and enables identification of Littrow wavelengths, as shown in Fig. 7(h). The modeled shift of the fringes can be

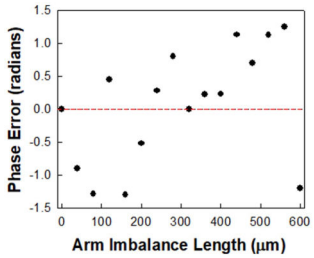


Fig. 8. Phase errors on the different arms of the FTS calculated from measured data in Interconnect simulation model (assuming a fixed trapezoidal waveguide geometry with bottom width 490 nm, height 230 nm and sidewall etch angle 85-degrees).

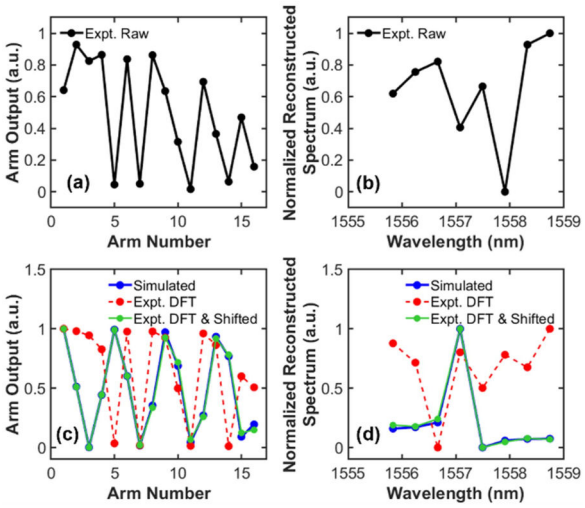


Fig. 9. (a) Raw experimentally measured interferogram from the 16 arms of the LT-MZI FTS with the corresponding spectral reconstruction in (b). (c) Experimentally measured power at 1557 nm (red) after DFT correction and (green) after DFT correction and phase shifting. Simulated power shown in blue. (d) Reconstructed spectra from interferograms in (c).

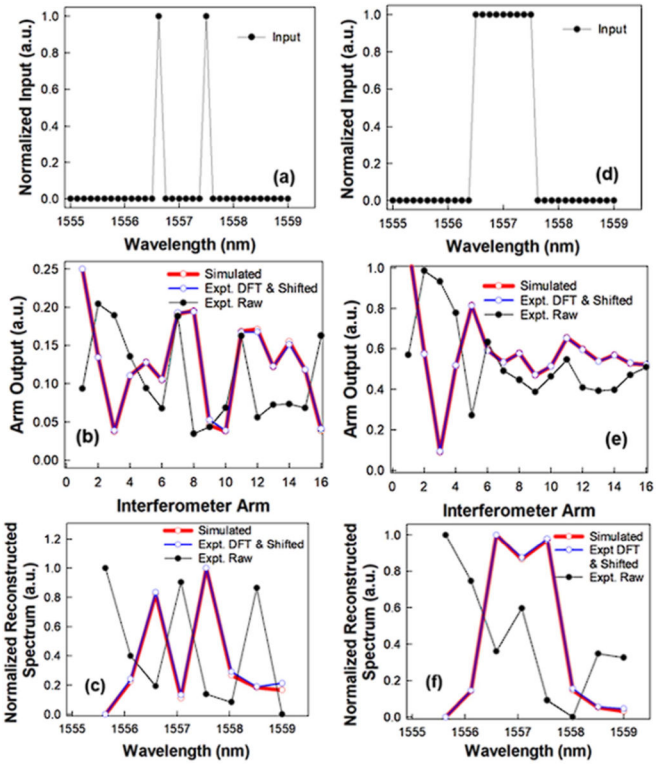


Fig. 10. Simulated (a) dual and (d) broadband input into the designed FTS. Power outputs that would result from the hypothetical inputs in (a) and (d), on the 16 interferometer arms are shown in (b) and (e) for simulated interference fringes, raw experimental measured fringes, and for the measured experimental fringes that are subsequently DFT corrected and phase shifted. (c) And (f) shows the normalized reconstructed spectra for corresponding cases in (b) and (e).

implemented in hardware based on achievable $\Delta\lambda$ simulated in Fig. 4, from the amorphous-crystalline phase transformations in $Sb_2Se_3$.

Once the Littrow condition is established, the input spectrum can be retrieved using the discrete Fourier transform method described in Section II, as shown in Fig. 9. Fig. 9(a) shows the raw measured power at $\lambda = 1557$nm from the 16 LT-MZI arms. The corresponding retrieved spectrum is shown in Fig. 9(b) which shows deviation from the expected spectral reconstruction from simulations. However, if we correct fringe amplitudes by DFT correction, and correct for phase errors from the estimated values in Fig. 8, the power would be measured correctly on the interferogram outputs and are seen to match with simulation results in Fig. 9(c). Fig. 9(d) can then accurately reconstruct the input spectrum from the corrected power which matches well with the known input. For sensors where a single resonance wavelength [15] or fringe minimum [16] needs to be identified, with change in refractive index of the analyte interacting with the sensor in biosensing or chemical sensing, the resonance wavelength and/or fringe minimum shifts can be determined effectively by our designed device.

An analysis for broadband spectroscopy is however challenging experimentally in our present devices where PCMs have still not been integrated. Due to uncertainties in mode effective index associated with variation in waveguide geometry across a wafer in foundry fabricated devices, we need to apply software-based phase error correction. While the effect of GCs, MMI cavity effects, Fabry-Perot effects and detector noise are removed via DFT data processing here, ensuring tight control on fabrication is necessary to ensure that the FSR in Fig. 4(f) can be reliably estimated and phase correction applied to all interferometer arms.

Once fringes are offset experimentally by PCM integration to align to a Littrow condition and DFT correction applied to amplitude-correct the fringes, the input spectrum can be reconstructed within the narrow band FSR of our designed FTS. To establish our hypothesis, we consider two hypothetical input sources comprising (1) two isolated wavelengths and (2) a broadband input as shown in Fig. 10(a) and (d) respectively. Fig. 10(b) and (e) show the expected as-measured output power and the corresponding output powers that would be measured on the interferometer arms once DFT correction of the interference fringe transfer functions is done, and phase correction is applied with PCMs. Fig. 10(c) and (f) show that once DFT correction and phase correction are applied, the corresponding input spectral

frequencies can be reliably discerned within the narrowband FSR of our demonstrated FTS, which is sufficient for applications tracking changes in a single resonance wavelength or interference fringe minimum. The small deviation observed between simulations and expected experimental results with the hypothetical sources in Fig. 10 once PCMs are integrated and corrections applied, is due to the fact that waveguide dispersion was ignored, and an average waveguide dimension was assumed. While these are sufficiently valid assumptions within the narrow band FSR of our FTS, for wider wavelength ranges, waveguide dispersion must be incorporated into the calculations, to accurately reconstruct the input spectra [27], [28], similar to the principle demonstrated in [13] with centimeter long interferometers with off-chip fringe detection.

To compensate for temperature effects, phase errors can be estimated similar to Fig. 8 for temperatures over the expected temperature range of interest in a field environment and stored in a database. The appropriate phase error table can be looked up from a database based on on-chip temperature feedback [29]. The alignment will incorporate the thermo-optic coefficients of silicon, silicon dioxide and integrated phase change materials from the measured LT-MZI transmission. The incorporation of PCMs thus pre-calibrates the Littrow wavelengths at a fixed temperature thus reducing one element of uncertainty during field measurements with no active power consumption. With respect to loss, silicon waveguide propagation loss at $<2$ dB/cm results in a maximum propagation loss difference between the shortest and longest interferometer at $<0.24$ dB. Effects of loss in longer unbalanced arms for higher FTS resolution can be mitigated in low-loss silicon nitride waveguides that have demonstrated losses $\sim$0.06 dB/cm. However, as we noted, effects of loss can be compensated by DFT processing the fringe interference transfer functions on the individual arms to the respective grating coupler envelopes.

Integration of PCMs with silicon photonic waveguides has been extensively demonstrated in the literature [19], [20]. While PCMs have not been integrated yet into our silicon photonic devices here, a standard process flow would involve the PCMs being deposited by reactive ion sputtering and the phase change enabled either optically or by electro-thermal heating from current flowing in an annealed transparent conducting film such as indium tin oxide (ITO) or titanium doped indium oxide (ITiO). The PCM would be encapsulated within a thin aluminum oxide film above the fabricated silicon photonic waveguides, that would provide good thermal conductivity while also preventing material loss during the melt-quench processes in the amorphous to crystalline phase transformations and vice-versa.

## V. Conclusion

In summary, we experimentally demonstrated a narrowband on-chip FTS based on spatial heterodyning using planar waveguide loop-terminated Mach-Zehnder interferometers. Our proof-of-concept studies show that LT-MZI FTSs can achieve $2\times$ better wavelength resolution than MZI based planar waveguide FTSs MZIs with the same geometric path length difference of the interferometer arms when resolving single frequency lineshapes and enables more compact on-chip FTSs. Our proposed method can enhance resolution and compactness in optical switch based FTSs demonstrated in MZI configuration [30]. Our non-volatile, in-situ non-thermal phase correction method can be applied in diverse applications such as optical delay lines [31] in diverse communication applications and resonance trimming in computing [32] and sensing applications [15], [16]. We showed that foundry fabricated waveguide geometry variations challenge the spectral reconstruction and proposed a method for post-fabrication narrowband correction in foundry fabricated FTSs with PCMs that accurately reconstructs the frequency spectra of single wavelength, dual wavelength and broadband input sources within the narrow band FSR. The PCM integration concept can be extended to correct phase errors in AWG spectrometers. The LT-MZI FTS concept can be extended to Sagnac Interferometer (SI) FTSs to reduce component phase errors by eliminating the second MMI ($\mathrm{MMI_B}$) with additional compactness. While the wavelength resolution of our proof-of-concept devices demonstrated here is 0.48 nm, future devices will integrate fine resolution compact LT-MZI and SI FTS in chip-based narrowband single wavelength/frequency biosensing and gas sensing with electrically set PCM tuned interference fringes.

## References


[1] C. Pasquini, "Near infrared spectroscopy: A mature analytical technique with new perspectives - A review," *Analytica Chimica Acta*, vol. 1026, pp. 8–36, Oct. 2018, doi: 10.1016/j.aca.2018.04.004.

[2] A. Rygula, K. Majzner, K. M. Marzec, A. Kaczor, M. Pilarczyk, and M. Baranska, "Raman spectroscopy of proteins: A review," *J. Raman Spectrosc.*, vol. 44, no. 8, pp. 1061–1076, 2013, doi: 10.1002/jrs.4335.

[3] Z. Zhang, Y. Wang, and H. K. Tsang, "Ultracompact 40-channel arrayed waveguide grating on silicon nitride platform at 860 nm," *IEEE J. Quantum Electron.*, vol. 56, no. 1, Feb. 2020, Art. no. 8400308, doi: 10.1109/JQE.2019.2951034.

[4] K. Ma, K. Chen, N. Zhu, L. Liu, and S. He, "High-resolution compact on-chip spectrometer based on an echelle grating with densely packed waveguide array," *IEEE Photon. J.*, vol. 11, no. 1, Feb. 2018, Art. no. 4900107, doi: 10.1109/JPHOT.2018.2888592.

[5] M. Faraji-Dana, E. Arbabi, A. Arbabi, S. M. Kamali, H. Kwon, and A. Faraon, "Compact folded metasurface spectrometer," *Nature Commun.*, vol. 9, no. 1, Oct. 2018, Art. no. 4196, doi: 10.1038/s41467-018-06495-5.

[6] D. Pohl et al., "An integrated broadband spectrometer on thin-film lithium niobate," *Nature Photon.*, vol. 14, no. 1, pp. 24–29, 2020, doi: 10.1038/s41566-019-0529-9.

[7] M. Florjańczyk, P. Cheben, S. Janz, A. Scott, B. Solheim, and D. X. Xu, "Multiaperture planar waveguide spectrometer formed by arrayed Mach-Zehnder interferometers," *Opt. Exp.*, vol. 15, no. 26, pp. 18176–18189, Dec. 2007, doi: 10.1364/OE.15.018176.

[8] D. González-Andrade et al., "Broadband Fourier-transform silicon nitride spectrometer with wide-area multiaperture input," *Opt. Exp.*, vol. 46, no. 16, pp. 4021–4024, Aug. 2021, doi: 10.1364/OL.438361.

[9] H. Wang, Z. Lin, Q. Li, and W. Shi, "On-chip Fourier transform spectrometers by dual-polarized detection," *Opt. Exp.*, vol. 44, no. 11, pp. 2923–2926, 2019, doi: 10.1364/OL.44.002923.

[10] S. N. Zheng et al., "Microring resonator-assisted Fourier transform spectrometer with enhanced resolution and large bandwidth in single chip solution," *Nature Commun.*, vol. 10, no. 1, May 2019, Art. no. 2349, doi: 10.1038/s41467-019-10282-1.

[11] H. Xu, Y. Qin, G. Hu, and H. K. Tsang, "Scalable integrated two-dimensional Fourier-transform spectrometry," *Nature Commun.*, vol. 15, no. 1, pp. 436–455, Jan. 2024, doi: 10.1038/s41467-023-44518-y.

[12] M. Iqbal et al., "Label-free biosensor arrays based on silicon ring resonators and high-speed optical scanning instrumentation," *IEEE J. Sel. Top. Quantum Electron.*, vol. 16, no. 3, pp. 654–661, May/Jun. 2010, doi: 10.1109/JSTQE.2009.2032510.

[13] M. C. M. M. Souza, A. Grieco, N. C. Frateschi, and Y. Fainman, "Fourier transform spectrometer on silicon with thermo-optic non-linearity and dispersion correction," *Nature Commun.*, vol. 9, no. 1, pp. 665–672, Feb. 2018, doi: 10.1038/s41467-018-03004-6.

[14] D. Weidmann, G. Wysocki, C. Oppenheimer, and F. K. Tittel, "Development of a compact quantum cascade laser spectrometer for field measurements of $CO_2$ isotopes," *Appl. Phys. B*, vol. 80, no. 2, pp. 255–260, 2005, doi: 10.1007/s00340-004-1639-7.

[15] S. Chakravarty et al., "Multiplexed specific label-free detection of NCI-H358 lung cancer cell line lysates with silicon based photonic crystal microcavity biosensors," *Biosensors Bioelectron.*, vol. 43, pp. 50–55, May 2013, doi: 10.1016/j.bios.2012.11.012.

[16] J. Shen, D. Donnelly, and S. Chakravarty, "Slow-wave-enhanced on-chip loop-terminated Mach-Zehnder interferometer sensor," *Opt. Lett.*, vol. 48, no. 22, pp. 5968–5971, Nov. 2023, doi: 10.1364/OL.500033.

[17] A. Li and Y. Fainman, "Integrated silicon Fourier transform spectrometer with broad bandwidth and ultra-high resolution," *Laser Photon. Rev.*, vol. 15, no. 4, 2021, Art. no. 2000358, doi: 10.1002/lpor.202000358.

[18] Z. Fang et al., "Ultra-low-energy programmable non-volatile silicon photonics based on phase-change materials with graphene heaters," *Nature Nanotechnol.*, vol. 17, no. 8, pp. 842–848, Aug. 2022, doi: 10.1038/s41565-022-01153-w.

[19] Y. Zhang et al., "Myths and truths about optical phase change materials: A perspective," *Appl. Phys. Lett.*, vol. 118, no. 21, 2021, Art. no. 210501, doi: 10.1063/5.0054114.

[20] C. Ríos et al., "Ultra-compact nonvolatile phase shifter based on electrically reprogrammable transparent phase change materials," *PhotoniX*, vol. 3, no. 1, pp. 26–38, 2022, doi: 10.1186/s43074-022-00070-4.

[21] H. Zhu, Y. Lu, and L. Cai, "Wavelength-shift-free racetrack resonator hybrided with phase change material for photonic in-memory computing," *Opt. Exp.*, vol. 31, no. 12, pp. 18840–18850, Jun. 2023, doi: 10.1364/OE.489525.

[22] H. Podmore, A. Scott, and R. Lee, "On-chip compressed sensing Fourier-transform visible spectrometer," *IEEE Photon. J.*, vol. 10, no. 6, Dec. 2018, Art. no. 6602010, doi: 10.1109/JPHOT.2018.2876657.

[23] A. V. Velasco et al., "High-resolution Fourier-transform spectrometer chip with microphotonic silicon spiral waveguides," *Opt. Lett.*, vol. 38, no. 5, pp. 706–708, Mar. 2013, doi: 10.1364/OL.38.000706.

[24] G. Finco et al., "Monolithic thin-film lithium niobate broadband spectrometer with one nanometre resolution," *Nature Commun.*, vol. 15, no. 1, Mar. 2024, Art. no. 2330, doi: 10.1038/s41467-024-46512-4.

[25] K. Takada, H. Aoyagi, and K. Okamoto, "Correction for phase-shift deviation in a complex Fourier-transform integrated-optic spatial heterodyne spectrometer with an active phase-shift scheme," *Opt. Lett.*, vol. 36, no. 7, pp. 1044–1046, Apr. 2011, doi: 10.1364/OL.36.001044.

[26] M. Delaney, I. Zeimpekis, D. Lawson, D. W. Hewak, and O. L. Muskens, "A new family of ultralow loss reversible phase-change materials for photonic integrated circuits: $Sb_2S_3$ and $Sb_2Se_3$," *Adv. Funct. Mater.*, vol. 30, no. 36, 2020, Art. no. 2002447, doi: 10.1002/adfm.202002447.

[27] L. Mertz, "Auxiliary computation for Fourier spectrometry," *Infrared Phys.*, vol. 7, no. 1, pp. 17–23, 1967, doi: 10.1016/0020-0891(67)90026-7.

[28] M. L. Forman, W. H. Steel, and G. A. Vanasse, "Correction of asymmetric interferograms obtained in Fourier spectroscopy," *J. Opt. Soc. Amer.*, vol. 56, no. 1, pp. 59–63, 1966, doi: 10.1364/JOSA.56.000059.

[29] A. Herrero-Bermello et al., "Temperature dependence mitigation in stationary Fourier-transform on-chip spectrometers," *Opt. Lett.*, vol. 42, no. 11, pp. 2239–2242, Jun. 2017, doi: 10.1364/OL.42.002239.

[30] D. M. Kita et al., "High-performance and scalable on-chip digital Fourier transform spectroscopy," *Nature Commun.*, vol. 9, no. 1, Oct. 2018, Art. no. 4405, doi: 10.1038/s41467-018-06773-2.

[31] W. Ke et al., "Digitally tunable optical delay line based on thin-film lithium niobate featuring high switching speed and low optical loss," *Photon. Res.*, vol. 10, no. 11, pp. 2575–2583, 2022, doi: 10.1364/PRJ.471534.

[32] S. Ohno, R. Tang, K. Toprasertpong, S. Takagi, and M. Takenaka, "Si microring resonator crossbar array for on-chip inference and training of the optical neural network," *Amer. Chem. Soc. Photon.*, vol. 9, no. 8, pp. 2614–2622, 2022, doi: 10.1021/acsphotonics.1c01777.